The final publication is available at

https://doi.org/10.1016/j.nima.2018.12.056

Additional Information

Novel Method to Measure the Intrinsic Spatial Resolution in PET Detectors Based on Monolithic Crystals

Andrea González-Montoro[a*], Filomeno Sánchez[a], Peter Bruyndonckx[b], Gabriel Cañizares[a], Jose M. Benlloch[a], and Antonio J. González[a]

[a] Instituto de Instrumentación para Imagen Molecular (I3M), CSIC — Universitat Politècnica de València, 46022 Valencia, SPAIN

[b] Preclinical Imaging, Bruker BBIO, BELGIUM

Abstract

The main aim of this work is to provide a method to retrieve the intrinsic spatial resolution of a gamma-ray detector block based on monolithic crystals within an assembled scanner. This method consists on a discrimination of the data using a software collimation process. The results are compared with an alternative method of separating two detector blocks far enough to produce a "virtual" source collimation due to the geometric constraints on the allowed coincidence event angles.

A theoretical model has been deduced to fit the measured light distribution profiles, allowing estimating the detector intrinsic spatial resolution. The detector intrinsic spatial resolution is expected to follow a Gaussian distribution and the positron-emitter source shape, given the small size of a ^{22}Na source with 0.25 mm in diameter, can be assumed to follow a Lorentzian profile. However, the collimation of the data modifies the source shape that is no longer a pure Lorentzian distribution. Therefore, the model is based on the convolution of a Gaussian shaped distribution (contribution of the detector) and a modified Lorentzian distribution (contribution of the collimated source profile) that takes into account the collimation effect.

Three LYSO crystals geometries have been studied in the present work, namely a 10 mm thick trapezoidal monolithic block, and two rectangular monolithic blocks with thicknesses of 15 mm and 20 mm, respectively. All the blocks have size dimensions of 50 mm × 50 mm. The experimental results yielded an intrinsic detector spatial resolution of 0.64±0.02 mm, 0.82±0.02 and 1.07±0.03 mm, for the 10 mm, 15 mm and 20 mm thick blocks, respectively, when the source was placed at the center of the detector. The detector intrinsic spatial resolution was moreover evaluated across one of the axis of each crystal. These values worsen to an average value of 0.68±0.04 mm, 0.90±0.14 and 1.29±0.19 mm, respectively, when the whole crystal size is considered, as expected. These tests show an accurate method to determine the intrinsic spatial resolution of monolithic-based detector blocks, once assembled in the PET system.

Keywords: Gamma ray detectors, Positron Emission Tomography, Intrinsic spatial resolution, SiPM array, Monolithic blocks

---

[*] Corresponding author. e-mail: andrea.gm@i3m.upv.es.

1. Introduction

33   In the field of Nuclear Medicine, Positron Emission Tomography (PET) scanners are widely used. They

34 provide quantitative functional information of the subject under study. In order to record the 511 keV gamma

35 rays resulting from the positron-electron annihilation, these scanners have been typically based on scintillation

36 crystal arrays [1]. However, in recent years, the interest of using PET detector blocks based on monolithic

37 crystals has increased. This interest is reflected not only from the academic point of view [2]-[6], but also from

38 the commercial one [7]-[9]. The main advantages of continuous crystals, such as the characterization of the light

39 distribution [10][11], the estimation of the gamma ray impact coordinates [12]-[14], or its spatial, energy and

40 time resolution capabilities [15]-[19], have been widely described elsewhere. One of the most important benefits

41 concerning the use of continuous blocks, in contrast to pixelated crystals, is the possibility to estimate the photon

42 depth of interaction (DOI) coordinate without the need of extra photosensors or scintillator material [20]-[25].

43   The intrinsic spatial resolution of detector blocks based on crystal arrays is typically given by the system

44 capabilities to resolve all crystal elements [21][22]. Also, it is related to the signal-to-noise ratio, provided by the

45 peak-to-valley ratio in flood images resolving these pixel elements. However, when monolithic crystals are used,

46 accurate determination of the intrinsic spatial resolution is challenging. In those crystals, the detector spatial

47 resolution is limited by several factors such as detector size, photosensor type and distribution, photon DOI and

48 scatter events, to name but a few. These factors cannot easily be isolated and studied experimentally. For this

49 reason several works have focused on exploring the resolution limits through Monte Carlo simulations or other

50 models [26]-[28]. Other factors, namely the non-collinearity of the annihilated photons or the positron

51 annihilation range, contribute to the reconstructed image resolution and are not taken into account when referring

52 to the detector itself. However, it should be pointed out that if the intrinsic detector spatial resolution is

53 determined by using positron emitters, then in addition to the source size, the positron annihilation range of the

54 source must be taken into account.

In detectors based on continuous crystals, it has been suggested obtaining the intrinsic spatial resolution by having a reference detector at a far distance generating a narrow gamma-ray beam. This technique has been used not only in the PET field [16], but also in other areas of research such as Astrophysics [29]. However, this is not easily applicable for two main reasons. First, long separation distances are required and, therefore, in order to have enough statistics, high activity sources or long measuring times are needed. Second, this is impracticable if the intrinsic detector resolution is aimed to be obtained once the PET scanner is assembled. Other methods are based on using physical collimators (tungsten or lead) with small apertures. However, using collimators increases the measurement time and produces a magnification effect of the source profile at the entrance face of the scintillator block (proportional to the collimator thickness) that has to be taken into account when calculating the detector intrinsic resolution.

The aim of this work is twofold. We demonstrate a method to measure the detector intrinsic spatial resolution of a PET system when the scanner is already assembled. The method we are proposing is based on software collimation of the data, thus, avoiding the need of moving away one of the detectors. In the following, we will refer to this method as "software collimation". We have compared the proposed method against the aforementioned "distant detector" approach. The second topic is about modelling the expected measured resolution profile. This model includes the essential processes contributing to the shape of the measured resolution profile. When a fitted model has converged to the measured resolution profile, the FWHM of the intrinsic resolution PDF can be extracted.

2. Materials

2.1. Monolithic scintillators

The monolithic crystal blocks under study are composed of LYSO material. Three different detector block geometries have been tested, namely a trapezoidal (50 mm × 50 mm exit face, 47.9 mm × 47.9 mm entrance face) block with a thickness of 10 mm [5], and two rectangular blocks (50 mm × 50 mm base) with thicknesses of 15

1   mm [30], and 20 mm [23], see Fig. 1 left, center and right, respectively. For all the scintillation blocks, all faces

2   are polished and the lateral ones black painted. The entrance face is coupled to a retro-reflector (RR) layer [23].

3   The RR layer is composed of several corner-cubes structures that are made of three-sided prisms (mutually

4   perpendicular) and reflect light back directly towards the source, displaced a small distance (120 μm), but

5   preserving the light distribution shape. The use of these devices has a positive impact on the spatial resolution as

6   demonstrated in [23][30][31]. For a given LYSO geometry, two identical detector blocks have been used in

7   coincidence mode, one of them working as the reference detector.

8
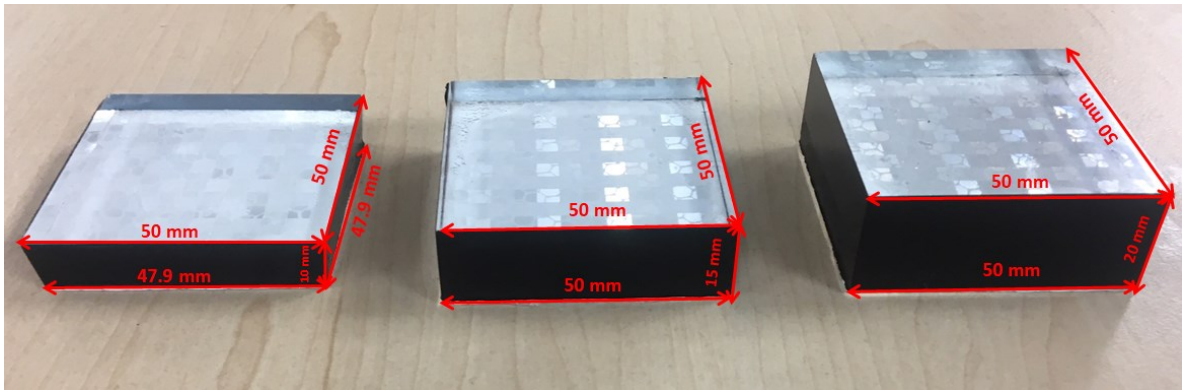
9   Fig. 1. Photograph of the three LYSO monolithic blocks used for the experiments. Left,
10 trapezoidal block 10 mm thick. Center, rectangular block 15 mm thick. Right, rectangular block
11 20 mm thick. The retroreflector layer coupled to the entrance face of the blocks can be seen
12 through the crystals.

13 *2.2. Photosensor and readout*

14 Custom photosensor arrays composed by 16×16 SiPMs (Silicon Photomultipliers) with 3×3 mm^2 active area

15 each (SensL, Cork, Ireland), and a pitch of 3.26 mm, were used. The SiPM matrix is operated at a bias voltage of

16 29 V, 4.5 V over the breakdown voltage [1]. Each SiPM has been connected to a readout circuit that provides

17 outputs for each row and column of the photosensor matrix [32]. The row and column readout electronics allow

18 one to characterize the light distribution (LD) originated from the interaction of a gamma ray within the

19 monolithic scintillator. The projection of the LD onto the X and Y axes makes it possible to determine the planar

20 X and Y coordinates, and also the photon DOI (Z coordinate).

2.3. Radioactive source

The ^{22}Na radioactive source used across all the experiments has a spherical shape with 0.25 mm in diameter and placed in the center of a PMMA encapsulation with 6 mm height and 25.4 mm in diameter. The activity of the source was low, about 7.4 kBq and, therefore, pile-up events due to high rates are not expected.

3. Methods

The readout electronics of each detector module provides digitized information of the LD projections for both X and Y axes [1][5][23][30]. In order to improve the calculation of the X and Y impact positions near the crystal edges, the centroids of these distributions are calculated through the center of gravity algorithm rose to a power of 2 [33]. The photon impact DOI is estimated by the ratio of the sum of all 16 signals (photon energy, E) to the maximum signal value $(E/I_{max})_{r,c}$ for row and columns (r,c) [23]. The final DOI value is assigned to the mean value of (E/I_{max}) obtained for r and c.

For all measurements the detector blocks temperature was monitored using sensors on the rear part of the SiPMs boards, remaining almost constant at 17±1 °C. No significant variations in the photopeak channel were found due to temperature variations. The energy resolution calculated as $\Delta E(FWHM)/E_{centroid}$ was also monitored for regions of interest around the measured radioactive source (around 3 mm × 3 mm) and found to be stable with an average value of 13±1 %, 14±1 % and 17±1% for the 10, 15 and 20 mm thick blocks, respectively. An energy window of 15% (434-588 keV) was applied to all data.

3.1. Intrinsic resolution measurements

In the following we describe the two main set-up configurations used in this work, see Fig. 2 (a)-(b). The first set-up shows the method for which one detector is moved far away. The opposite detector is sequentially moved from the detector under study from a distance of 115 mm up to 1780 mm in order to measure the resolution as a function of the collimation angle. There is no significant influence of the source size on the determined

1   collimation angle (about 0.5% maximum) or due to the non-collinearity of the annihilation photons (maximum

2   0.3%) for the distances we have considered. In this case, the natural Line of Response (LOR) collimation angle is

3   a function of the distance between the two detectors and, therefore, can be calculated as:

4   $$\theta_{DD} = atan\frac{x}{S_d} \qquad\qquad (1)$$

5   where x is the half of the reference detector crystal size, 25 mm in our case, and S_d is the separation distance

6   between the reference detector and the source. Here we did not perform any type of collimation. By moving away

7   the reference detector we are "naturally" collimating the source, and therefore, isolating the source contribution

8   to the measured spatial resolution FWHM of the detector under study. The acquisition time was increasing as a

9   function of the separation distance between the modules in order to retrieve similar overall counts for all

10 distances ($\sim 2\times 10^5$ coincidences). A coincidence window of 5 ns was selected. The data acquisition system has

11 been described elsewhere, see for instance references [5][23].

12 The second set-up, as depicted in Fig. 2 (b), describes the method we are proposing. Here we fixed the

13 distance between the two detector blocks to 115 mm. We acquired during 15 minutes recording $\sim 2\times 10^6$

14 coincidences whereas in the previous method we need to acquire at least 90 minutes for the longest separation

15 distance recording a factor ten less coincidences. In this case, software collimation is applied to the data. The

16 software collimation varies as a function of the LOR angle, and consists on allowing only events whose LOR has

17 a slope smaller than a predefined one. For each coincidence we calculate the angle between its LOR and the

18 normal ($\theta_{software}$), see Fig. 2 (b). If $\theta_{software}$ is smaller than the selected collimation angle, the event is accepted. The

19 system accepts events from squared regions under this angular restriction. Events in each detector block are

20 binned in 600×600 pixels. In particular, we have configured collimation angles varying from 0.001 radians to

21 nearly 0.2 radians from the normal, corresponding to squared regions in the reference detector of 0.23 mm and

22 46.60 mm, respectively. Smaller collimation angles were not considered because of the lack of statistics. In

23 contrast to the distant detectors set-up, in the proposed method only one measurement is needed.

1   To study the intrinsic detector resolution across the whole crystal surface, the source was displaced in steps of

2   1 mm from one border of the crystal to its center, assuming a symmetrical behavior of the other half. Each data

3   point was software collimated in the range of 0.001 rad to 0.2 rad.
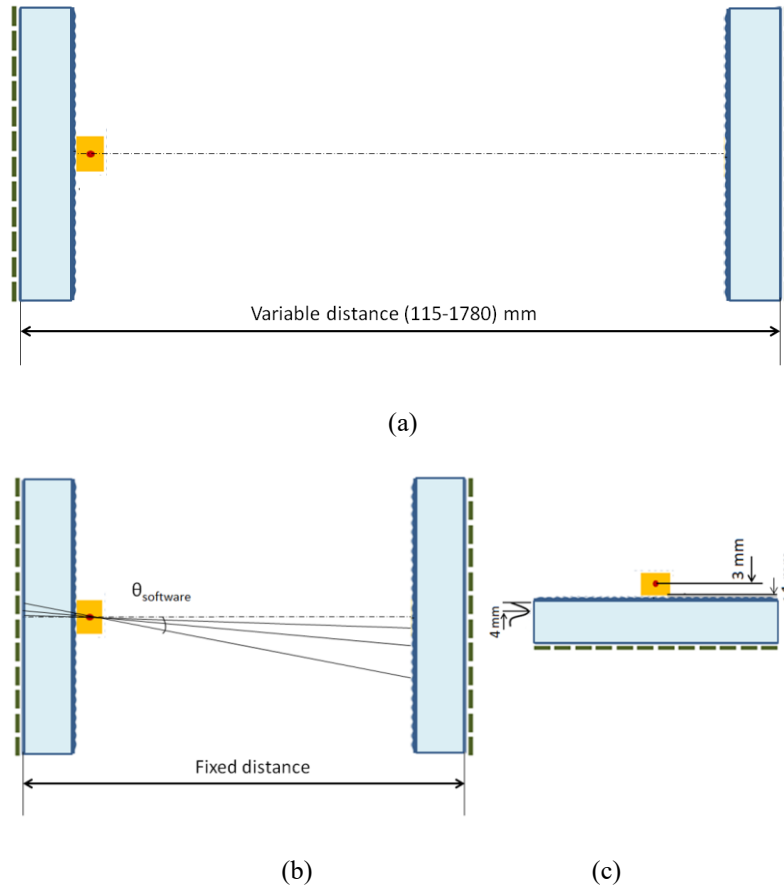

(a)

(b)   (c)

Fig. 2. Sketch of the experimental setups. Both detectors included a monolithic LYSO crystal with black painted lateral walls and were read out using an array of 16×16 SiPMs. (a) Distant detectors method showing the small size source of ^{22}Na in front of the detector under study. (b). Software Collimation method. (c) Sketch showing the distance from the source to the scintillator active volume. It is also depicted the most probable DOI, about 4 mm, in a 10 mm thick LYSO crystal.

3.2. Source simulation

Using GATE, a simulation platform based on the Geant4 Application for Tomographic Emission [34], we have carried out simulations of the ^{22}Na source profiles in order to deduce the expected contribution of the

1   positron annihilation range to the experimental measurements. The simulated source is a [22]Na sphere of 0.25 mm

2   in diameter inside a PMMA disk (12.7 mm radius, 6 mm thick). In these simulations, in contrast to the default

3   parameters in GATE for this source, the whole energy distribution of the [22]Na positron emission was considered

4   and not only the maximum energy value. Figure 3 shows the energy spectra considered for the [22]Na source

5   together with the spectra of other isotopes of interest in PET scanners. This distribution was calculated following

6   an analytical expression valid for allowed or super allowed beta decays [27][35]. The theoretical energy

7   distribution is of the form:

8    $$N(E)dE = gF(Z, E)pE(E_{max} - E)^2 dE \qquad (2)$$

9   where $N(E)$ is the number of decays at energy E, g is a coupling constant, E is the β particle energy, E_{max} is the

10   maximum energy of that particles (0.545 MeV for [22]Na), p is its momentum, $F(Z, E)$ is the Fermi function, and Z

11   is the atomic number of the beta decay daughter. A non-relativistic approximation for the Fermi function, valid

12   for allowed transitions of lighter elements is [38][39]:

13 $$F_{allowed}(Z, E) = 2\pi \frac{\eta}{(1 - e^{-2\pi\eta})} \qquad (3)$$

14   where $\eta = -Z\alpha E/p$ for positron decays, and $\alpha = 1/137$, the fine structure constant.

15
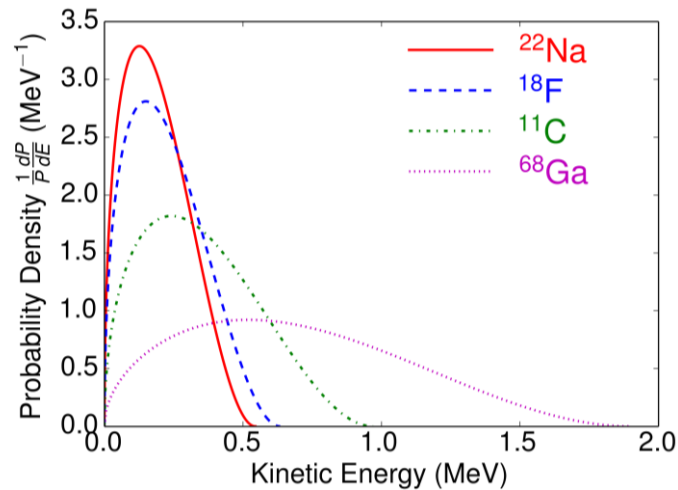
16   Fig. 3. β^+-decay energy spectra for different isotopes of interest for PET studies. In particular, the
17   solid red line shows the energy spectra of the [22]Na source used in this study. The energy curve
18   for the ^{68}Ga has also been calculated (dotted pink line), as it is not also found by default.

1   The simulation contour plot and the profile of the annihilation points of the source are shown in Fig. 4 (a) and

2   (b), respectively. We have performed fits to these profiles with both Gaussian and Lorentzian distributions.

(a)   (b)
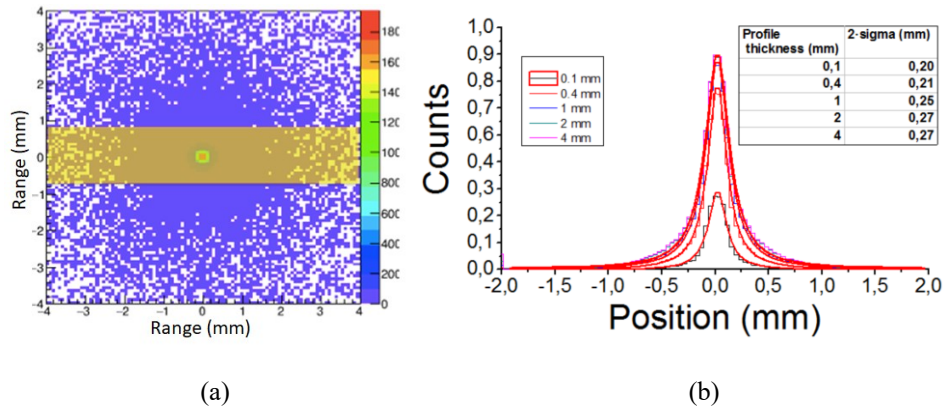
Fig. 4. (a) Contour plot for the simulated ^{22}Na 0.25 mm source. (b) Simulated profiles (see
yellow band in panel (a)) and fits carried out using a Lorentzian distribution. Profiles for
different band widths ranging from 0.1 mm to 4 mm were studied.

9   Better agreement is achieved when using Lorentzian functions, with 0.99 regression coefficients. The

10 Lorentzian FWHM of the fitted profiles will be used in the following to estimate the intrinsic detector spatial

11 resolution. The analysis of the experimental data is done by studying a 1D projection of the 2D projections of the

12 annihilation point distribution. The thicknesses of the projection bands have been studied since those slightly

13 impact the resulting Lorentzian FWHM, see Fig. 4. For band widths wider than 1 mm, the determined FWHM

14 remains constant at 0.27 mm. For a very thin band with a width of only 100 μm, the difference from 4 mm bands

15 is smaller than 30 %, see Table 1. We have finally selected a Lorentzian FWHM of 0.27 mm for the ^{22}Na source,

16 which corresponds to the value found for profile thicknesses 2-4 mm.

17 Table 1. Lorentzian FWHM of the source profile for different band widths.

Band width (mm)	FWHM (mm)
0.1	0.20
0.4	0.21
1	0.25
2	0.27
4	0.27

18

3.3. Data analysis

During the data analysis we have characterized the measured profiles of the small size source. In order to provide accurate determination of the width of the measured profiles, those need to be given in metric units. For this purpose, the radioactive source was displaced across the crystal surface at known positions. The observed source in the flood maps are projected onto the X and Y axis, see example in Fig. 5 (a)-(b). We have projected bands of several pixels, typically 10 pixels corresponding to approximately 1.6 mm, onto the X and Y axes. Smaller bands widths have also been tried with insignificant differences in the results.

The relation between the measured position in channels and the known geometrical beam position fits well to a first order polynomial, in the central crystal region. However, in order to account for the truncation of the light distribution at the crystal edges that renders compression of the events in this region, a third order polynomial fit is better suited [23]. Figure 6 (a), (b) and (c), show the mechanical curve versus the measured positions obtained for the three different scintillators. The thicker crystal (20 mm) suffers from a larger truncation of the data at the crystal edges, which explains why the 20 mm thick crystal curve shows a more accused compression. The plots show the bias, which is the deviation between the mechanical and the measured source position, across the crystal surface. For the 10 mm thick crystal, the bias is smaller than in the 15 mm and 20 mm thick crystals, as expected. For the thickest crystal case, due to the stronger light truncation, the bias is larger in the extrema, about 6 mm. However, these effects do not constrain the current results allowing characterizing events in the whole surface.

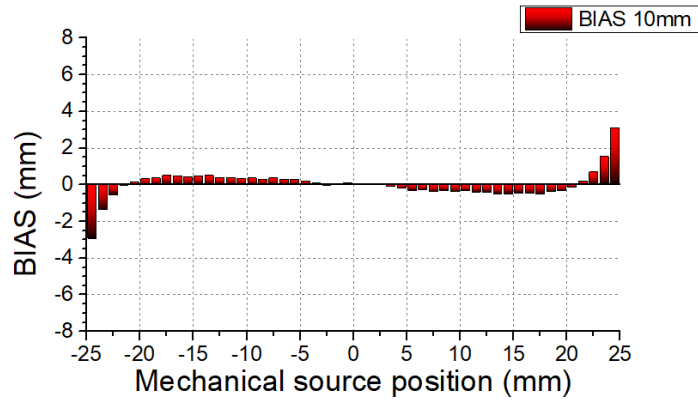(a)   (b)
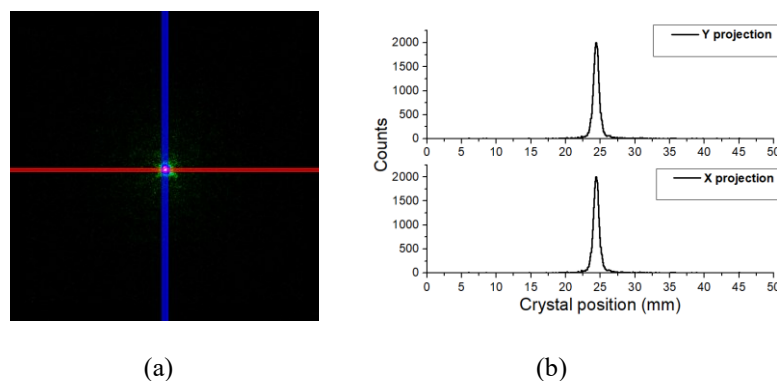
Fig. 5. (a) Flood map of the image with the point-like source in the center of the 10 mm thick block 600 × 600 pixels. (b) Two projections (X and Y) for the blue and red bands depicted in (a).
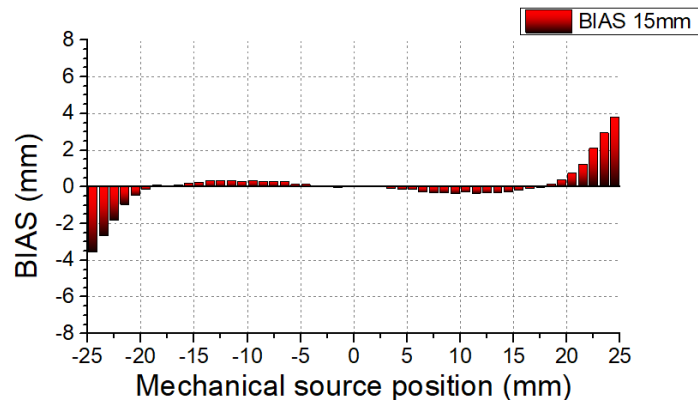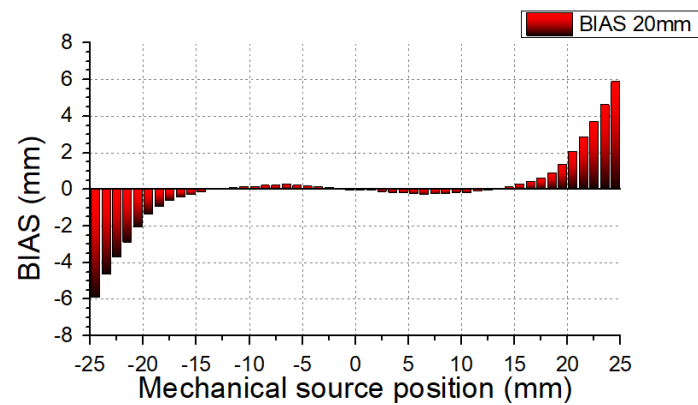
1

(a)

(b)

(c)

Fig. 6. Deviation between the known mechanical and measured source position across the crystal surface for (a) the 10 mm, (b) the 15 mm, and (c) the 20 mm thick blocks, respectively.

1   *3.4. Extracting the intrinsic resolution*

2   The main objective is to provide a model that can be used to determine the detector intrinsic resolution by

3   fitting the measured source profiles. The detector intrinsic spatial resolution is convolved with the source

4   dimension resulting on the measured $FWHM_{measured}$. If both, detector and source, were to follow Gaussian

5   distributions, the resulting $FWHM_{measured}$ could be expressed as $\sqrt{FWHM_{source}^2 + FWHM_{detector}^2}$, which is the

6   usual way of dealing with this entangle. Indeed, this approach works well when the source dimensions are large

7   and therefore closer to a Gaussian distribution. However, in this work we aim to isolate as much as possible the

8   source contribution from the detector under analysis and, therefore, a very small size source was used (0.25 mm

9   in diameter).

10   Assuming that the positron-emitter source follows a Lorentzian profile and the detector intrinsic resolution

11   follows a Gaussian distribution, it turns out that the convolution of these distributions is the so-called Voigt

12   function [36], which cannot be evaluated in closed form and therefore has to be evaluated numerically. However,

13   in our case there is a collimation effect that produces a broadening of the source distribution. For that reason the

14   convolution of the detector Gaussian shaped distribution and the "collimated" source profile is no longer a Voigt

15   distribution.

16   Therefore, the profiles of the projected 1D collimated beam images (see Fig. 5b) contain three essential

17   contributions namely, i) the distribution of the gamma emission points in the positron source; ii) the influence of

18   the gamma beam created by the software collimation; and iii) the intrinsic detector resolution. To disentangle the

19   effect of these three components, a mathematical model of the measured beam profiles was developed which

20   takes into account the contribution of each of them. In this work we assume that the intrinsic resolution PDF is

21   Gaussian with a FWHM characterizing the intrinsic resolution. This intrinsic resolution PDF has to be convolved

22   with the normalized intensity distribution of the gamma emission points in the ^{22}Na point source and the software
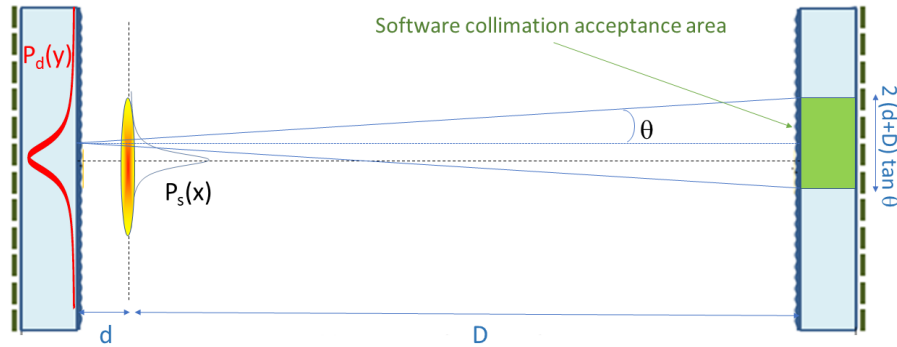
23   collimation method.

Fig. 7. Schematic drawing showing the nomenclature employed in the mathematical beam
profile model used to extract the intrinsic resolution.

3.4.1 Combined influence of source distribution and software collimation

The probability that a gamma emitted by the emission point distribution $P_s(x)$ of the ^{22}Na source hits the detector surface at a point y at a distance d from the source (see Fig. 7), while fulfilling the software collimation constraint (i.e. the angle between the LOR connecting the impact point on the detector under study and the 2nd detector at a distance D from the source used to perform the software collimation, is smaller than a given collimation angle θ) can then be expressed as:

$$P_d(y) = \frac{1}{C} \int_{-\infty}^{\infty} P_s(x) \cdot B\left(y + (x - y) * \frac{d+D}{d}, y, 2 * (d + D) * \tan(\theta)\right) dx \qquad (4)$$

where θ is the maximum photon incidence collimation angle allowed in the monolithic block, C is a constant defined such that $P_d(y)$ is a PDF and therefore its integral over all possible y values should be 1 and the function $B(x, c, w)$ represents the software collimation effect and is defined as aun unit box function with its center at c and has a width w, that can be defined as:

$$B(x, c, w) = \begin{cases} 0 \ if \ x < c - w/2 \\ 1 \ if \ c - w/2 \leq x \leq c + w/2 \\ 0 \ if \ c + w/2 < x \end{cases} \qquad (5)$$

In section 3.2 it has been shown that the 1D gamma emission point distribution $P_s(x)$ of the ^{22}Na source used in the experimental set-up can be modelled with a Lorentzian distribution with a $FWHM_{source}$ of 0.27 mm.

$$P_s(x) = \frac{2}{\pi \cdot FWHM_{source}\left(1 + \frac{4x^2}{FWHM_{source}^2}\right)} \qquad (6)$$

1   Evaluating the integral in eq. 4 then can be shown that the effect of the software collimation procedure

2   produces a 1D Probability Density Function (PDF) of photons impact position y on a plane at a distance d from

3   the source that can be expressed as:

4    $PDF(y|d, FWHM_{source}, \theta) =$

5    $\frac{1}{\pi \cdot K} \cdot \left(tan^{-1} \left(\frac{2y}{FWHM_{source}} + \frac{2d \tan(\theta)}{FWHM_{source}} \right) - tan^{-1} \left(\frac{2y}{FWHM_{source}} - \frac{2d \tan(\theta)}{FWHM_{source}} \right) \right)$ (7)

6   where K is a normalization constant given by:

7    $K = \int_{-\infty}^{\infty} \frac{1}{\pi} \left(tan^{-1} \left(\frac{2(y + d \tan(\theta))}{FWHM_{source}} \right) - tan^{-1} \left(\frac{2(y - d \tan(\theta))}{FWHM_{source}} \right) \right) = 2\, d\, tan(\theta)$ (8)

8   We will refer to θ as $\theta_{software}$ when referring to the software collimation method and θ_{DD} for the distant

9   detector method. Since the gammas do not interact at the surface of the detector but penetrate to different depths,

10   the final gamma interaction distribution in the detector is given by a weighted average of the

11   $PDF(y|d, FWHM_{source}, \theta)$ at different interaction depths z in the detector:

12   $\int_{d_{min}}^{d_{max}} e^{-\mu \cdot (z - d_{min})} * PDF(y|d, FWHM_{source}, \theta) \cdot dz$ (9)

13   In the above equation, it was assumed that the front of the detector is at a distance of d_{min} from the source

14   while d_{max} is equal to d_{min} + detector thickness. Therefore, the d parameter takes into account the distance from

15   the source to the impact position within the scintillator material. The average interaction depth $\bar{d}$ within the

16   crystal can be theoretically estimated as a cone with opening angle θ [37]:

17   $\bar{d} = \frac{cos\theta}{\mu} + \frac{L}{1 - e^{\frac{\mu L}{cos\theta}}}$ (10)

18   where μ is the attenuation coefficient of the LYSO material at 511 keV (0.87 cm^{-1}), and L is the crystal thickness.

19   We obtain values of $\bar{d}$ of about 4.2 mm, 5.6 mm and 7.2 mm from the entrance surface for the 10 mm, 15 mm

20   and 20 mm thick crystals, respectively. Since there are 3 mm source encapsulation (half thickness) + 0.5 mm

21   housing + 0.5 mm retroreflector + ~ 0.5 mm spacing between the source edge and the detector housing, see Fig. 2

22   (c), d is estimated to be about 9±1 mm, 10±1mm and 12±1 mm for each crystal respectively.

1   3.4.2 Software collimation model limitations

2   In the model, to predict the gamma interaction point distribution probability at a given distance d from the

3   point source, the effect of multiple interactions (i.e. a Compton scatter followed by a photoelectric absorption or a

4   second Compton scatter in the same block) is neglected. However, in a real experiment, gammas that undergo

5   multiple interactions will have a measured position that is usually (much) further away from the collimated beam

6   center in comparison to single interaction events. When small software collimation angles are used, many of

7   these multiple interaction events will be rejected for analysis and hence the model remains valid for most events

8   in a measured data set.

9   Regarding gamma-rays impinging closer to the crystal edges, i.e. when the collimated beam is moved very

10   close to the edge of the two opposite blocks, the gamma interaction point distribution probability gets truncated at

11   one side. This effect was not put in the current model because no analytical solution of equation 7 could be found

12   in this case. Hence the contribution of the beam collimation in the last 1 or 2 mm from the edge can be slightly

13   overestimated. However, for small collimation values there is almost no influence of this effect on the data and

14   therefore, since the model takes into account all the collimated profiles we do not expect a significant impact in

15   the final resolution value.

16   3.4.3 Adding the intrinsic resolution contribution to the measurement model

17   To model the final profile of the measured data we convolved the source Lorentzian modified profile

18   (i.e. $PDF(y|d, FWHM_{source}, \theta)$) with the Gaussian intrinsic detector resolution point spread function (PSF),

19   characterized by a standard deviation σ. This resulted on the final resolution model given by:

20     $$f(xy|d, FWHM_{source}, \theta, \sigma) =$$

21     $$\frac{cot\theta}{2\pi d} \cdot \sum_{n=0}^{1}(1-2n) \cdot \left(\frac{\pi}{2} Re(Erf(z_n)) - Im\left\{z_n^2 \, {}_2F_2\left(1,1;\frac{3}{2},2;-z_n^2\right)\right\}\right) \quad (11)$$

22   with

23     $$z_n = \frac{2d \cdot (1-2n) \cdot \tan(\theta) + i \cdot FWHM_{source} + 2y}{2\sqrt{2}\sigma} \quad (12)$$

1   *Re* and *Im* are operators that take the real and imaginary parts respectively. *Erf* and $_2F_2$ represent the Error and a

2   generalized hypergeometric functions, respectively. This equation was fitted simultaneously to measure the

3   resolution profiles taken at eight different collimation angles (from 0.009 up to 0.08 radians) where the effect of

4   the different depth of interactions on the final distribution can be considered negligible. For large collimation

5   angles, the shape of the weighted average PDF is very different compared to the PDFs at a specific distance.

6   Hence, the deduced equation cannot be used reliably in these cases. For small to medium collimation angles the

7   shape of the weighted average PDF remains similar to the shape of the PDFs at a specific distance. Since the

8   intrinsic spatial resolution is independent of the collimation angle, σ was taken as a common parameter in the

9   simultaneous fits. $FWHM_{source}$ was fixed at 0.27 mm, as was derived from simulations, while the distance d was

10 left as a free parameter to fit in order to verify if its value would converge close to the expected average

11 interaction depths.

12 **4. Results**

13   *4.1. Validation of the software collimation method*

14   We have first validated the proposed method of software collimating the data with the most traditional one of

15 sequentially moving backwards the detector for coincidences. The validation test was carried out for the 10 mm

16 thick LYSO crystal and with the source positioned at its center.

17   Figure 7 shows the $FWHM_{measured}$ as a function of the collimation angle for both the distant detector approach

18 (open circles), and the proposed software collimation method (full squares). Notice that we have not carried out

19 any photon DOI selection to the data. We selected projections in the flood maps (600×600 pixels) of the source

20 onto the X and Y axes. Each data point is calculated as the average of the $FWHM_{measured}$ for the X and Y profiles.

21 The $FWHM_{measured}$ is obtained by fitting the measured data to Gaussian distributions. This is a good

22 approximation to the alternative way of calculating the maximum value of the distribution and measuring the

23 width at the half of that maximum for each profile. We have checked this assumption by manually measuring the

1   width of several profiles. Good agreement was obtained for all crystal geometries, obtaining deviations smaller

2   than 2% and, thus, validating the Gaussian fitting procedure. The error bars associated to each point are

3   calculated as the standard deviation of the two (X and Y) Gaussian FWHM to each profile.

4   A good agreement between the two collimation methods was observed, as depicted in Fig. 8. In the following

5   section both data sets have been fitted using the proposed model, retrieving identical detector intrinsic resolution

6   values. Notice that whereas in the distant detectors method the number of counts is similar for all collimation

7   angles, in the software collimation method the statistics are being reduced as a function of the angle due to the

8   reduction in the accepted number of counts.

9
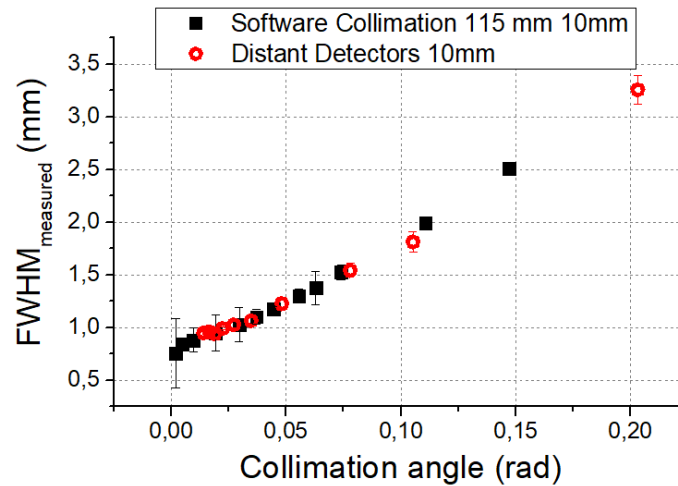
10
11 Fig. 8. Validation of the proposed method (software collimation, full squares) compared to the
distant detector method (open circles) for the 10 mm thick crystal.

12 *4.2. Gamma interaction distribution and source modelling*

13   As we have already pointed out, the gammas do not interact at the detector surface but penetrate to different

14   depths within the scintillator block. Therefore, the final gamma interaction distribution in the detector is modelled

15   using Eq. 9. Figure 9 shows the modelled source distribution in the detector for the 10 mm thick block. These

16   results show the PDFs for different collimation angles and at different depths overlapping with the weighted

17   average PDF (black solid line, assuming the front of the detector is 4.5 mm away from the source, i.e. d_{min}=4.5

18   mm in Eq. 9). For large collimation angles, the shape of the weighted average PDF is very different compared to

1   the PDFs at a specific distance. Hence, Eq. 9 cannot be used reliably in these cases. However, for small and

2   medium collimation angles the shape of the weighted average PDF remains similar to the shape of the PDFs at a

3   specific distance. For this reason we are considering angles ≤ 0.1 radians for the model.

4   To find out the average interaction distance at which Eq. 9 matches best with the weighted averaged PDF, we

5   have plotted the variation of the integrated absolute difference between the weighted averaged PDF and PDFs at

6   a specific depth. Figure 10 shows these values for two different collimation angles. For the 10 mm thick crystal

7   the best agreement is achieved at a depth of 9±1 mm from the source, corresponding to approximately 5±1 mm

8   DOI from the crystal entrance. Using Eq. 10 we estimated an average interaction distance of 9±1 mm (i.e. 4.2

9   mm DOI), which agrees well with the obtained value.

10
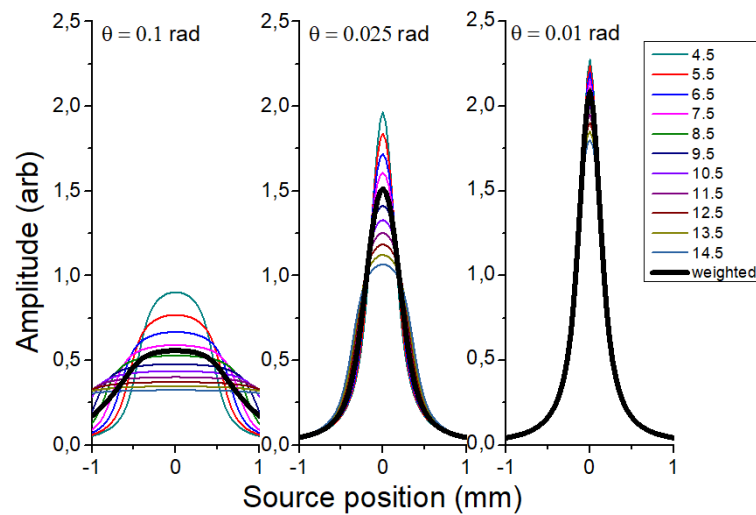
11   Fig. 9. PDFs at individual depths (in mm) in comparison with the weighted average PDF (black
12   solid line) for three different collimation angles (in radians). The profiles are obtained for the 10
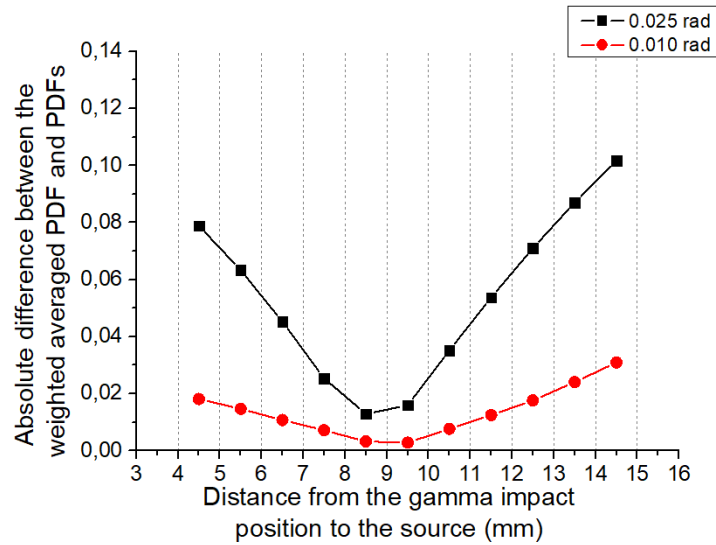13   mm thick block.
14

Fig. 10. Integrated absolute difference between the averaged PDF and a PDF at a specific interaction distance from the source for the 10 mm thick block.

4.3. Modelling of the measured resolution profiles. Fitting analysis

We have fitted the measured source profiles for the different collimation angles using Eq. 11 and Eq. 12. The fitting returns the source-detector distance, the $FWHM_{source}$ and the detector intrinsic resolution. Notice that Eq. 11 is not completely valid for large collimation angles, so we avoid using profiles whose collimation angle is $\geq$ 0.1 radians. The profiles for all collimation angles are simultaneously fitted using Eq. 11, sharing the free detector intrinsic resolution parameter. The source size contribution ($FWHM_{source}$) was also shared but fixed at 0.27 mm, as earlier predicted by simulations. The data obtained for the smallest collimation angle was not included due to the lack of statistics. The number of angular samples considered for the fitting was 6; using ± 1 samples we did not observe significant changes. Table 2, summarizes the angular range considered for each crystal.

1   Table 2. Angular range considered for each studied crystal.

Scintillator thickness (mm)	Angular range (radians)
10	0.009-0.08
15	0.009-0.08
20	0.009-0.07

2

3   We have first validated the model with the measurements performed at the crystals center. The fitting of both

4   the X and Y profiles was performed using Wolfram Mathematica [40]. The fitting procedure yields a detector

5   intrinsic resolution FWHM of 0.64±0.02 mm for the 10 mm thick crystal when using the software collimation

6   data. The data obtained when using the distant detector set-up was also analyzed using the same methodology

7   resulting on a comparable detector intrinsic resolution FWHM of 0.65±0.03 mm, therefore, confirming the

8   robustness of the software collimation set-up. Once the software collimation method was validated with the 10

9   mm thick block, identical data sets were acquired using the software collimation set-up for the 15 mm and 20 mm

10   thick blocks. The analysis of the data returned values of 0.82±0.02 mm and 1.07±0.03 mm FWHM, respectively.

11   Note that the detector intrinsic resolution FWHM was estimated as the average value of both the X and Y

12   profiles. The quoted uncertainty corresponds to the standard deviation between the X and Y profiles.

13   These analyses also provided information on the distance between the source and the interaction point of

14   7.9±0.2 mm, 9.0±0.3 mm and 11.1± 0.4 mm for the 10 mm, 15 mm, and 20 mm thick blocks, respectively. These

15   results agree well with the expected values estimated using Eq. 10. Figure 11 shows in black circles the measured

16   profiles and with a red line the model prediction for the 10 (top), 15 (central) and 20 (bottom) mm thick blocks,

17   and for three different collimation angles. A good agreement between the measured profiles and the model is

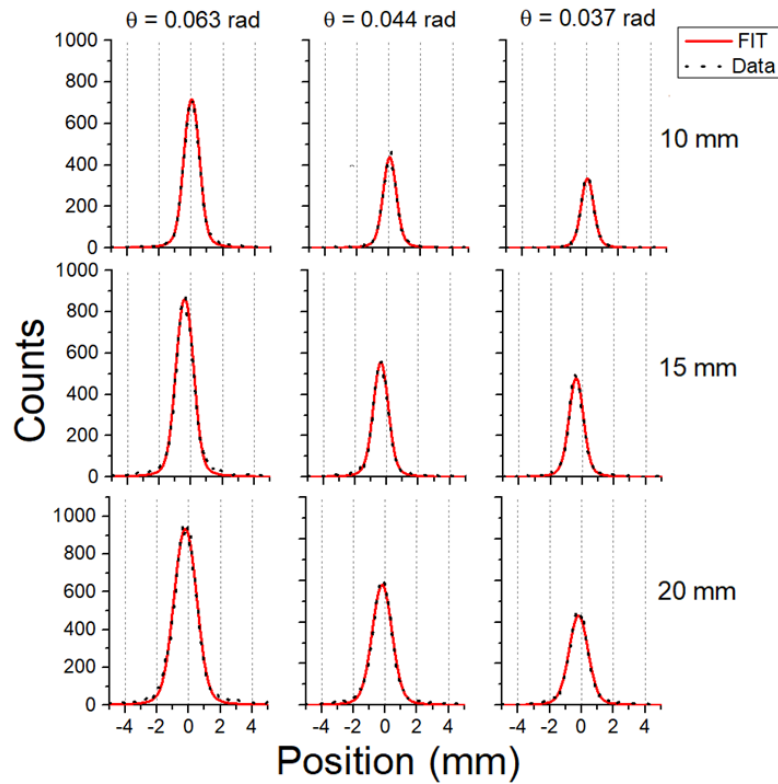18   observed for each collimation angle.

19

Fig. 11. Measured profiles (black points) and model prediction (red line) for three collimation angles (in radians). Top, profiles for the 10 mm thick crystal. Central. Profiles for the 15 mm thick crystals. Bottom, profiles for the 20 mm thick crystal.

4.4. Impact position dependence

The acquired profiles have been analyzed using the proposed model in order to obtain the dependence of the detector intrinsic spatial resolution with the impact position. Here, the $FWHM_{source}$ was again fixed to 0.27 mm and d was left as a free parameter. Figure 12 shows the detector intrinsic spatial resolution FWHM as a function of the mechanical source position. In order to take into account the influence of the crystal edges and since we moved the source across the x-axis of the detector, we have calculated the resolution values for the X profiles of the source. The variation of the calculated detector intrinsic spatial resolution FWHM with the impact position is larger for the 15 and 20 mm thick crystal cases. This is produced because the thicker crystals produce a stronger truncation of the LD and, thus, a worse characterization of its centroid position (see Fig. 6) [11].

1   Table 3. Intrinsic detector spatial resolution (FWHM$_{detector}$) obtained for all scintillator geometries.

Scintillator	Central Source	Average [-20,20] mm	Average [-25,25] mm
10 mm	0.64±0.02	0.67±0.03	0.68±0.04
15 mm	0.82±0.02	0.85±0.06	0.90±0.14
20 mm	1.07±0.03	1.22±0.10	1.29±0.19

2
3

4
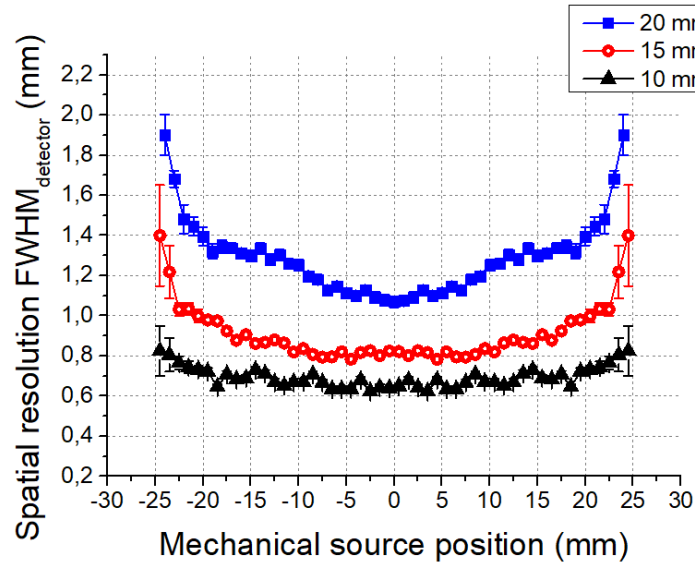
5   Fig. 12. Detector intrinsic spatial resolution FWHM as a function of the source mechanical
6   position. Black full triangles show the results for the 10 mm thick crystal, the red open circles
7   those for the 15 mm thickness and blue full squares are for the 20 mm thick block.
8
9   For data corresponding to the whole crystal surface, the mean detector intrinsic spatial resolution was found to

10   be 0.68±0.04 mm for the 10 mm case, slightly improving to 0.67±0.03 mm when the range is reduce to [-20, 20]

11   mm, since less truncation is observed. The 15 mm thick crystal exhibits an average intrinsic spatial resolution for

12   the whole crystal of 0.90±0.14 mm. This improves to 0.85±0.06 mm when the range is reduce to [-20, 20] mm.

13   Finally, the 20 mm thick crystal exhibits an average intrinsic spatial resolution for the whole crystal of

14   1.29±0.19 mm. This improves to 1.22±0.10 mm when the range is reduced to [-20, 20] mm. Table 3 summarizes

15   the average values for impacts only at the crystal center, for the range varying from -20 to 20 mm and when

16   considering the whole crystal surface from -25 to 25 mm.

1 **5. Discussion and conclusions**

2   We have proposed a method to determine the intrinsic detector spatial resolution in detector blocks based on

3   monolithic crystals suitable for PET systems. This approach can be done while the PET system is already

4   mounted and only requires one measurement. The method consists on software collimation of the measured data

5   in order to isolate the finite source size $FWHM_{source}$ contribution to the $FWHM_{measured}$. We have derived Eq. 11

6   that uses this information and returns the intrinsic detector spatial resolution together with the most suitable

7   distance between the source and the interaction depth within the scintillation block. The method has been

8   validated against the approach of using a bench-top set-up where the reference detector is sequentially moved

9   backwards, requiring a higher number of measurements and also a long separation distance between the detectors

10 in order to avoid the influence of the source size on the reference detector. We have found comparable results

11 when using the two experimental approaches, i.e. the proposed software collimation method and the geometrical

12 collimation using a bench set-up ("distant detector" approach), see Fig. 7.

13   This new experimental method allows obtaining the detector intrinsic spatial resolution by performing only

14 one measurement. However, this measurement should have enough statistics to allow applying small angular

15 restrictions without introducing significant statistical fluctuations. The proposed method is capable to provide the

16 intrinsic detector spatial resolution within an assembled PET scanner. In this work results for a fixed distance of

17 115 mm are shown regarding the case of the software collimation method. However, other distances have also

18 successfully been tested for this method retrieving the same results.

19   Averaged intrinsic detector spatial resolutions for the whole crystal surface, of 0.68±0.04 mm, 0.90±0.14 mm

20 and 1.29±0.19 mm have been obtained for the 10 mm, 15 mm and 20 mm thick crystals, respectively. The

21 intrinsic spatial resolution strongly depends on the detector block characteristics, such as the scintillator geometry

22 and the photosensor sampling matrix. In this case we are using a 16×16 SiPM matrix, 3.26 mm pitch. For SiPM

23 arrays with larger pitches or larger photosensor sizes we expect some degradation on the intrinsic spatial

24 resolution. As shown along this work, also the crystal geometry has an impact on the $FWHM_{measured}$, the thicker

25 the crystal the worse the $FWHM_{measured}$.

1   The measured profiles were fitted using a simplistic version of the model based on the so-called Voigt

2   function (see section 3.4). The main drawback of this model is that did not account for the influence of the

3   software collimation in the profiles and required *d* to be fixed for events towards the edges of the detector. An

4   underestimation of the detector intrinsic resolution of about 10% was observed when compared with the proposed

5   method [41]. Other works are based on determining the point spread function (PSF) of the whole scanner system

6   at the imaging space, (mainly based on Gaussian fits [42]) or at the projection space. In the last case, the system

7   response function can be determined through analytical derivations, Monte Carlo simulations, or empirically [43].

8   In theory, the empirical approach of physically measuring the system response to a collimated point source leads

9   to the most accurate description of the system [44]. However, as far as we know, no empirical determination of

10   the intrinsic spatial resolution at individual detector module elements has been reported. The accurate knowledge

11   of this individual intrinsic spatial resolution and its dependency with the impact position in the monolithic

12   detector surface allows one considering this information during the reconstruction process. For instance, one

13   could include this information in the reconstruction algorithms, expecting to produce an improvement on the

14   quality of the final image.

15 **References**

16 [1] M. Larobina, et al., "Small Animal PET: A Review of Commercially Available Imaging Systems", Current Medical Imaging
17   Reviews, 2, 187-192. August, 2014.
18 [2] D.R.Schaart, et al., "A novel, SiPM-array based, monolithic scintillator detector for PET" Physics in Medicine & Biology, Volume
19   54, Number 11. June, 2009.
20 [3] M.C. Maas, et al., "Experimental characterization of monolithic-crystal small animal PET readout by APD arrays" IEEE Trans.
21   Nucl. Sci., vol. 53, no. 3, pp. 1071-1077, June 2006.
22 [4] E. Yoshida, et al., "Basic performance of a large area PET detector with a monolithic scintillator" Radiological Physics and
23   Technology, Volume 4, Issue 2, pp 134–139. July, 2011.
24 [5] A.J. Gonzalez, et al., "A PET detector based on SiPM and Monolithic LYSO crystals: Performance Evaluation" IEEE
25   Transactions on Nuclear Science, vol: 63, Issue: 5, pp. 2471 – 2477. December, 2016.
26 [6] J. Cabello, et al "High resolution detectors based on continuous crystals and SiPMs for small animal PET" Nucl. Instrum. Methods
27   Phys. Res. A 718 148–50. December, 2013.
28 [7] F. Sanchez, et al., "ALBIRA: a small animal PET/SPECT/CT imaging system"; 40(5):051906. May, 2013.
29 [8] L. Moliner et al., Design and evaluation of the MAMMI dedicated breast PET, Med. Phys. Vol 39,no. 9(2012)5393-5404.
30 [9] P. Mollet, et al., "The β-CUBE, a high-end compact preclinical benchtop PET for total body imaging" J Nucl Med May 1, 2017
31   vol. 58 no. supplement 1 393.

[10] P. Conde, et al., "3-D photon impact determination using fitting approaches to the Light Distribution" Nuclear Science Symposium and Medical Imaging Conference (NSS/MIC), 2014 IEEE

[11] C.W. Lerche, et al., "Depth of γ-Ray Interaction Within Continuous Crystals From the Width of Its Scintillation Light-Distribution," Trans. Nucl. Scie, vol. 52, pp 560, 2005.,

[12] P. Bruyndonckx, et al., "Neural network-based position estimators for PET detectors using monolithic LSO blocks" IEEE Transactions on Nuclear Science, vol: 51, Issue: 5, October, 2004

[13] R. Pani, et al., "Position algorithm for monolithic scintillation crystals based on charge projection readout" Journal of Instrumentation, Volume 11, January 2016 .

[14] Z. Li, et al., "Nonlinear least-squares modeling of 3D interaction positioning in a monolithic scintillator block" Phys. Med. Biol. 55 6515, 2010.

[15] S. España, et al., "DigiPET: submillimeter spatial resolution small-animal PET imaging using thin monolithic scintillators" Phys.Med. Biol. 59 3405–20, 2014.

[16] P. Bruyndoncx, et al., "Study of the spatial resolution in gamma detectors using photosensitive wire chambers in view of their use as high resolution PET scanners" Nucl. Inst. Meth. Phys. Res. A323 (1992) 54-59

[17] R.S. Miyaoka, et al., "Resolution properties of a prototype continuous miniature crystal element (cMiCE) scanner" IEEE Trans. Nucl. Sci. 58 2244–9, 2011.

[18] R. Marcinkowski, et al., "Sub-millimetre DOI detector based on monolithic LYSO and digital SiPM for a dedicated small animal PET system" Phys. Med. Biol. 61 (2016) 2196–2212

[19] H.T. Van Dam, et al., "Sub-200 ps CRT in monolithic scintillator PET detectors using digital SiPM arrays and maximum likelihood interaction time estimation" Physics in Medicine & Biology, Volume 58, Number 10, 2013.

[20] R. Pani, et al., "A Novel Method for γ−photons Depth-of-Interaction Detection in Monolithic Scintillation Crystals" IEEE Transactions on Nuclear Science Volume: 63, Issue: 5, Oct. 2016

[21] J.R. Stickel, et al., "Fabrication and characterization of a 0.5-mm lutetium oxyorthosilicate detector array for high-resolution PET applications" J. Nucl. Med. 48 115–21, 2007.

[22] A. Chatziioannou, et al., "Detector development for microPET II: a 1 µl resolution PET scanner for small animal imaging" Phys. Med. Biol. 46 (2001) 2899–2910

[23] A. Gonzalez-Montoro, et al., "Performance Study of a Large Monolithic LYSO Detector with Accurate Photon DOI Using Retroreflector Layers," Trans. Rad. Plasma Med. Scie., in press. DOI: 10.1109/TRPMS.2017.2692819, 2017.

[24] X. Li, et al., "A high resolution, monolithic crystal, PET/MRI detector with DOI positioning capability" Engineering in Medicine and Biology Society, 2008

[25] A.J. Gonzalez, et al., "The MINDView brain PET detector, feasibility study based on SiPM array," Nucl. Instrum. Meth. A, vol. 818, pp. 82, 2016.

[26] J.R. Stickel, "High-resolution PET detector design: modelling components of intrinsic spatial resolution," Physics in Medicine and Biology, vol. 50, pp 179, 195, 2005.

[27] C.S. Levin. "Calculation of positron range and its effect on the fundamental limit of positron emission tomography system spatial resolution." Physics in Medicine and Biology, vol. 44, pp 781, 1999.

[28] W. Lehnert. "Analytical positron range modelling in heterogeneous media for PET Monte Carlo simulation." Physics in Medicine and Biology, vol. 57, pp 4075, 4076, 2011.

[29] D. Attie, et al., "INTEGRAL/SPI ground calibration" Astronomy & Astrophysics Letters 411(2003)71-80.

[30] A. González-Montoro, et al., Detector block performance based on a monolithic LYSO crystal using a novel signal multiplexing method, Nuclear Inst. and Methods in Physics Research, A (2018)

[31] A. Gonzalez-Montoro, et al., Highly improved operation of Monolithic BGO-PET blocks, Journal of Instrumentation, Volume 12, C11027, November 2017.

[32] A.V. Stolin, et al., "Evaluation of imaging modules based on SensL array SB-8 for nuclear medicine applications," IEEE Trans. Nucl. Sci., vol. 61, no. 5, pp. 2433–2438, Oct. 2014.

[33] R. Pani et al., "Continuous DOI determination by Gaussian modelling of linear and non-linear scintillation light distributions," in Proc. IEEE NSS-MIC, Valencia, Spain, 2011, pp. 3386–3389

[34] D. Strul, "GATE (Geant Application for Tomographic Emission): a PET/SPECT general-purpose simulation platform." Nuclear Physics B (Proc. Suppl.) vol. 125, pp. 75, 2003.

[35] R.D. Evans, "The atomic nucleus." Tata McGraw Hill Publishing Company Limited. 1955.

[36] J.J. Olivero and R.L. Longbothum, "Empirical fits to the Voigt line width: a brief review," J. Quant. Sprectrosc. Radiat. Transfer., vol. 17, pp. 233, 1977.

[37] A. Soriano, et al., "Minimization of Parallax Error in Dedicated Breast PET," Trans. Nucl. Scie., vol. 60, pp. 739, 2013.

[38] C.S. Wu and S.A. Moskowski, 1966 Beta Decay (New York: Interscience).

[39] H. Daniel, "Shapes of beta-ray spectra" Rev. Mod. Phys. 40 659–72, 1968.

[40] Wolfram Research, Inc., Mathematica, Version 11.3, Champaign, IL (2018).

[41] A. Gonzalez-Montoro et al., "A Method to Measure the Intrinsic Detector Resolution on Monolithic Crystals," in Proc. IEEE NSS-MIC, Atlanta, U.S.A, 2017.

[42] A. A. Attarwala, et al., "A Method for Point Spread function Estimation for Accurate Quantitative Imaging," Trans. Nucl. Scie., vol 65, pp 961-969.

[43] V.Y. Panin et al., "Fully 3-D PET Reconstruction With System MatrixDerived From Point Source Measurements", IEEE Transactions on Medical Imaging, vol. 25 (2006) 907-921.

[44] A.M. Alessio et al., "Modeling and Incorporation of System Response Functions in 3-D Whole Body PET", IEEE Transactions on Medical Imaging, vol. 25 (2006) 828-837.

Acknowledgments